Terahertz Kerr and reflectivity measurements on the topological insulator Bi$_2$Se$_3$

G. S. Jenkins, A. B. Sushkov, D. C. Schmadel, N. P. Butch, P. Syers, J. Paglione, and H. D. Drew

Center for Nanophysics and Advanced Materials, Department of Physics, University of Maryland, College Park, Maryland 20742, USA

We report the first terahertz Kerr measurements on bulk crystals of the topological insulator Bi$_2$Se$_3$. At T =10 K and fields up to 8 T, the real and imaginary Kerr angle and reflectance measurements utilizing both linearly and circularly polarized incident radiation were measured at a frequency of 5.24 meV. A single fluid free carrier bulk response cannot describe the line shape. Data from one sample is quantitatively described by a surface state with a small mass and surprisingly large associated spectral weight. However, an alternative interpretation in terms of bulk carrier-density variations remains a possibility

I. INTRODUCTION

The discovery[1–8] and realization of 3D strong topological insulators[9–12] have generated much recent interest. A strong spin-orbit coupling can produce a topologically protected metallic surface state which has a Dirac-type dispersion with a nondegenerate chiral spin state that cannot be destroyed or gapped by (nonmagnetic) impurity scattering. Since the spin direction of the quasiparticle is locked to the momentum direction,[10] suppression of Anderson localization results from the destructive interference associated with the quais-particle's Berry phase upon backscattering.[13] With the action of local ordered magnetic moments, the surface state becomes gapped.[7] In zero magnetic field with the Fermi energy within the gap, a quantized Kerr angle associated with the half-quantized Hall conductance is a predicted signature of the topological origin of the surface state.[7]

These and other predicted properties have stimulated a recent flurry of activity to probe the exotic surface state. Although the surface states have been observed by angle-resolved photoemission spectroscopy (ARPES),[9–12] unam-biguous separation of bulk from surface-state conduction has plagued transport characterization of the surface state due to the rather large intrinsic charge density in the bulk conduc-tion band in as-grown Bi$_2$Te$_3$ and Bi$_2$Se$_3$. Various schemes to circumvent this difficulty in bulk crystals have either imple-mented counterdoping during growth,[14] minimized Se vacancies[15] or fine-tuned annealing processes.[14] One inter-mediate goal has been to sufficiently deplete the bulk to al-low gating or chemical doping of the surface in suitably thin crystals to move the chemical potential of the bulk into the gap.[16]

There are several advantages of terahertz Kerr measure-ments over other transport measurements which allow sepa-ration of the surface from the bulk response. The surface states are expected to have a different mass than the bulk, depending on the location of the chemical potential, giving rise to two different resonant cyclotron frequencies. This ef-fect can be further exaggerated by application of an electric field either from gating or chemically doping the surface causing "band-bending" effects, pushing the Dirac point closer to the chemical potential. Second, the line shape as a function of magnetic field associated with a surface state is qualitatively different than the bulk response. Third, no elec-

trical contacts are required. Lastly, Kerr measurements on thick crystals allow probing of a single surface state.

In this paper, Kerr measurements are reported on two bulk crystals of Bi$_2$Se$_3$ at an optical frequency of 5.24 meV in fields up to 8 T. Line fits of the data on the sample with the lowest carrier concentration are quantitatively consistent with surface states. For a measured surface-state cyclotron mass of m_{cs}=0.033m_e, the associated spectral weight is about a factor of 20 times larger than expected based on the corre-sponding number density estimated from ARPES data. Mea-surements of other samples from the same as-grown crystal show a higher carrier concentration. Alternatively, a simple model of the optical response which assumes the presence of two crystallites with different carrier concentrations can qualitatively describe all of our data. Future work to opti-cally characterize carrier-density homogeneity as well as an analysis of surface-state signals expected by gating are discussed.

II. EXPERIMENTAL DESCRIPTION

A. Kerr system description and calibration

For calibration purposes, the Faraday rotation and ellip-ticity induced by a sample in magnetic field was measured utilizing a polarization modulation technique with a hetero-dyne detection scheme, a technique detailed elsewhere.[17] The complex Faraday angle and relative transmission were con-currently measured.

The instrument was modified allowing simultaneous mea-surement of the complex Kerr angle and relative reflection by the insertion of a beam splitter, polarizer, and collection optics which include an off-axis parabolic aluminum mirror and a 2 K silicon composite bolometer as depicted in Fig. 1. The Kerr and Faraday angles are measured separately.

Assuming a rotationally invariant sample, the complex Kerr and Faraday angles are defined as follows:

$$\tan(\theta_K) = i(r_+ - r_-)/(r_+ + r_-),$$

$$\tan(\theta_F) = i(t_+ - t_-)/(t_+ + t_-),$$

where r (t) is the reflection (transmission) complex Fresnel amplitude of the sample expressed in a circular polarization
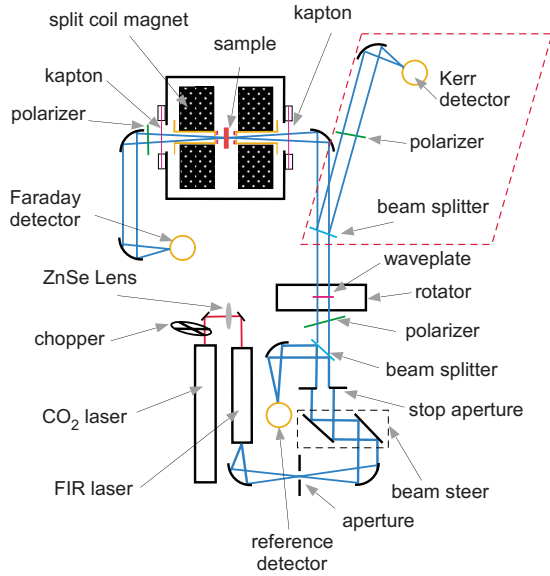
FIG. 1. (Color online) Schematic of the Faraday and Kerr optical system capable of operating on various laser lines in the terahertz spectral region. The figure, adapted from Ref. 17 which details the Faraday experiment, depicts additional optics within the red-dashed trapezoid allowing Kerr measurements by capturing reflected light from the sample.

basis. The + and − represent right and left circular polarization states, respectively.

Absolute measurement of the real part of the Faraday and Kerr angles is verified by inserting a linear polarizer into the

system immediately downstream from the rotator. The measured rotation angle equals the polarizer angle for small angles which is a very good approximation for the signals measured in Bi_2Se_3. Large angle calibration may be accomplished in a similar manner, but corrections from higher order terms involving the Fresnel amplitudes must be explicitly taken into account in the modulated signal.[17]

Calibration of the imaginary part of the Faraday and Kerr angles is accomplished by measuring the known response of a GaAs two-dimensional electron gas (2DEG) heterostructure. A NiCr antireflection (AR) coating was deposited on the backside to minimize multiple reflections within the GaAs substrate. There is a well-defined relationship between the real and imaginary parts of the Faraday angle as well as the Kerr angle. Therefore, the imaginary part may be calibrated against the real part. In this way, calibration of the system is performed as a function of magnetic field in the same manner as samples of interest without the addition of other optical components. Utilizing the formalism developed in Appendix A 2, the real and imaginary parts of the Faraday and Kerr angles data shown in Figs. 2(a)–2(d) are simultaneously fit where the mobility μ, cyclotron mass m, 2D number density n, and sheet resistance of the AR coating $R_\square$ are free parameters. The B-field value of the resonance determines the mass m, the width of the resonance determines the scattering rate characterized by the mobility μ, the overall strength of the response determines the number density n, and deviations of the AR coating sheet resistance $R_\square$ away from the ideal value tends to mix the real and imaginary parts of the angles giving rise to anisotropies in the resonant peaks.
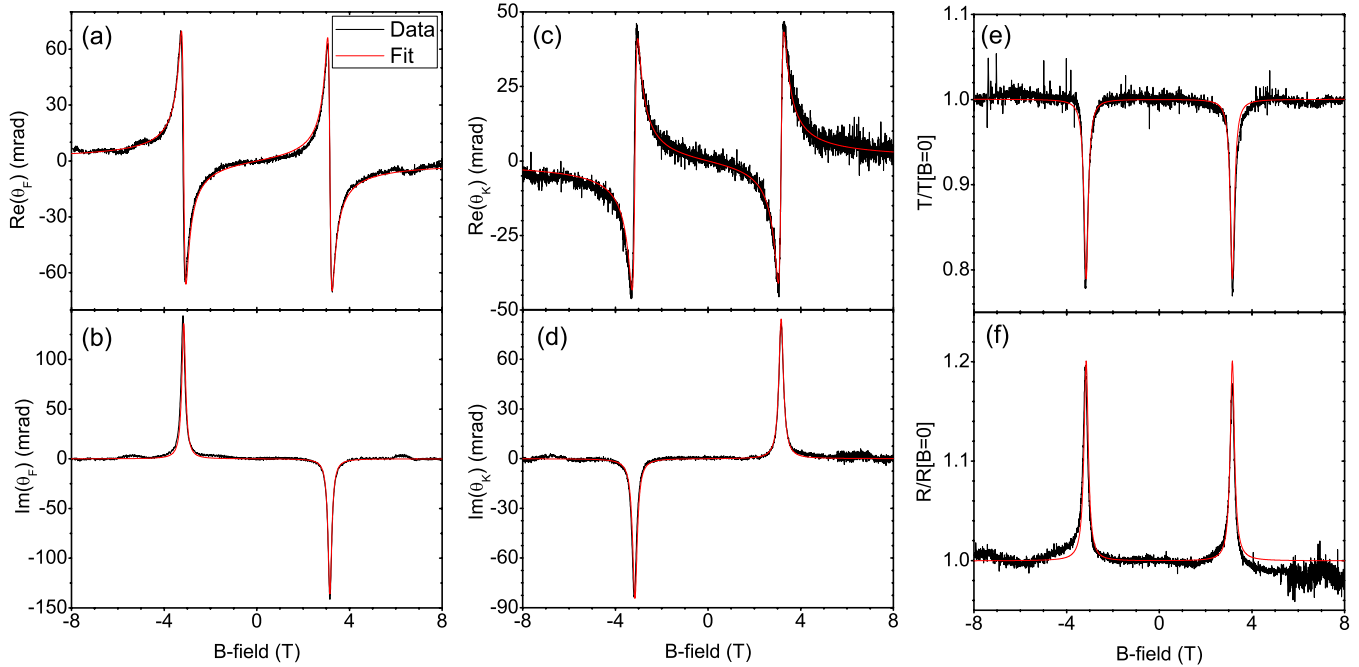

FIG. 2. (Color online) Calibration of the Faraday and Kerr angle measurement system. The Faraday angle, Kerr angle, and relative transmission and reflection from a GaAs 2DEG heterostructure were measured at an optical frequency of 5.24 meV and temperature of 80 K as a function of magnetic field. The Faraday and Kerr angles are simultaneously fit with effectively two parameters, the number density and mobility, found to be $n = 2.0 \times 10^{11}$ cm^{-2} and $\mu = -1.19 \times 10^5$ cm^2/V s. The fits (red line) are overlaid on top of the data (black dots) for comparison. The same two parameters are used to calculate reflection and transmission (normalized to the $B=0$ value) and overlaid on the data.
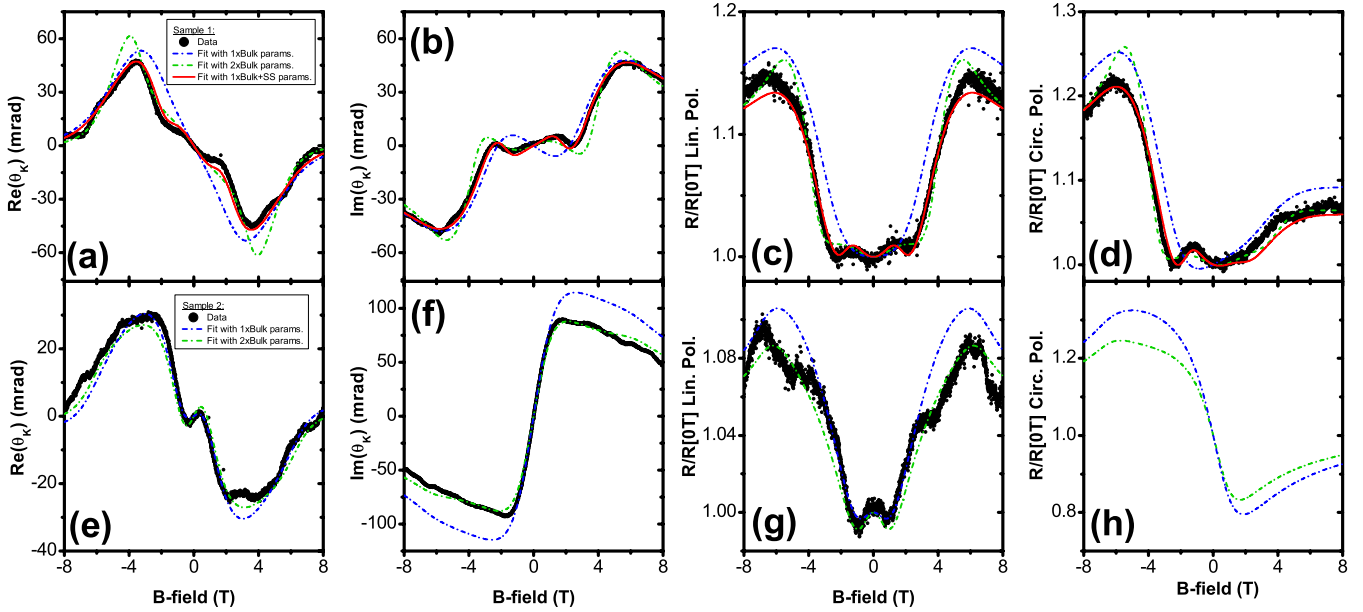
FIG. 3. (Color online) Kerr angle and reflection of linearly polarized light normalized to the $B=0$ T value were measured at 10 K and an optical frequency of 5.24 meV. Reflection of nearly circularly polarized light normalized to the $B=0$ T value was a separate measurement performed only on sample 1. [(a)–(d)] Sample 1 data (black dots) are depicted with several different fits superimposed. A homogeneous bulk response cannot describe the data (blue dashed-dotted). A homogeneous bulk response with surface states (red solid) fit the data. The weighted optical response of two crystallites with different carrier density (green dashed-dotted) can reproduce the salient features of the data. Slightly elliptically polarized light, characterized by parameter $\beta=0.13$, is used in calculations for Fig. 3(d). [(e)–(h)] Sample 2 data (black dots) show a very different response but was only 2 mm away from sample 1 in the as-grown crystal. A homogeneous bulk response (blue dashed-dotted) does not quite describe the data. Addition of a surface-state response does not improve the fits. A weighted response of two crystallites with different carrier density (green dashed-dotted) more closely resembles the data. No reflectivity data using circular polarized light was taken for sample 2. β is assumed zero in calculations in Fig. 3(h).

The fit parameters are found to be the following: $n=2.0 \times 10^{11}$ cm^{-2}, $\mu=-1.19\times10^5$ cm^2/V s where the negative sign denotes the sign of the carriers, $m=0.0695m_e$, and $R =1.01\times R_{AR}$, where m_e is the mass of an electron and R_{AR} is the sheet resistance for the perfect AR coating condition of GaAs given by $Z_0/(n_{GaAs}-1)=145$ $\Omega/\square$, where $Z_0 =377$ $\Omega/\square$ is the impedance of free space and $n_{GaAs}=3.6$ is the index of refraction for GaAs. The mass is consistent with the known mass of GaAs (Ref. 18) and the antireflection coating is very close to ideal. The fits are overlaid on top of the reflection and transmission data shown in Figs. 2(e) and 2(f). Essentially, all six curves are very well reproduced with only two parameters, n and μ. Together with the polarizer calibration, the 2DEG GaAs calibration indicates that both the Kerr and Faraday experiments perform exceptionally well.

This particular data set also illustrates the robustness of the Kerr system. Instability associated with the two-laser system occurred between +8 and ~+5.5 T appearing as a loss of power and commensurate increase in relative detector noise in the Kerr and reflection data sets. Although the reflection data were visibly affected, the Kerr signal was essentially unaffected. The reflection measurement is derived by the ratio of the signals from two detectors ("Kerr detector" and "reference detector" in Fig. 1) and therefore susceptible to large spacial mode fluctuations but the Kerr signal is derived from the modulated signal measured by a single detector.

B. Bi$_2$Se$_3$ sample description

Bulk crystals of Bi$_2$Se$_3$ were prepared by combining elemental Bi and Se in the ratio 2:3.3 in a sealed ampoule and heating to 850 C, followed by a slow cool.[15] Surfaces were cleaved perpendicular to the c axis, and the backsides were cut and ground yielding a total bulk thickness of about 0.5 cm. Samples were mounted such that the applied magnetic field was parallel to the c axis and the radiation propagation direction. The effective area measured was defined by the optical spot size $\sim\varnothing1.0$ mm. During a time span of about 10 s, the surfaces of the crystals were cleaved using scotch tape in air and immediately inserted into a vacuum of $\sim10^{-7}$ Torr.

III. KERR AND REFLECTION MEASUREMENTS ON Bi$_2$Se$_3$ AND MODEL DESCRIPTION

The Kerr angle and concurrent reflection measurements of linearly polarized light are shown in Figs. 3(a)–3(c) and 3(e)–3(g) for two samples both measured at 10 K in fields up to 8 T. A separate measurement was performed on sample 1 where the wave plate in the rotator depicted in Fig. 1 was statically set producing elliptically (nearly circularly) polarized light. The reflection was then measured and normalized to the $B=0$ T value. The data are reported in Fig. 3(d). β characterizes the degree of mixing between left and right circular polarization states via $(1-\beta)R_+ + \beta R_-$, where $R_\pm$ is

the reflection produced by purely circularly polarized light. In this measurement, β is found to be 0.13.

To analyze the results, a model is constructed where the bulk is considered to be a thick slab whose optical response is characterized by a dielectric function consisting of a Drude carrier response with an associated unscreened bulk plasma frequency ω_{pb}, bulk cyclotron mass m_{cb}, and bulk scattering rate γ_b along with the addition of two TO phonon modes whose parameters have been previously determined.[19] The surface state resides at the interface whose admittance is modeled within a Drude model with an associated 2D surface plasma frequency ω_{ps}, surface cyclotron mass m_{cs}, and surface scattering rate γ_s. Details of the model are discussed in Appendix A 3.

IV. DISCUSSION

A. Analysis of the optical response

Sample 1 data shown in Figs. 3(a)–3(d) cannot be quantitatively nor qualitatively reproduced by a homogenous bulk response with any arbitrary carrier concentration, cyclotron mass, or scattering rate. The blue dashed-dotted curves in Figs. 3(a)–3(d) show a representative example of line shapes expected from a simple bulk response, calculated with the specific parameters $\omega_{pb}=420$ cm^{-1} (corresponding to a number density of $n_b \sim 3.2 \times 10^{17}$ cm^{-3}), $\gamma_b=12$ cm^{-1}, and $m_{cb}=.135m_e$. Although the high field Kerr data in Figs. 3(a) and 3(b) is well described by this particular set of parameters, strong qualitative deviations exist at fields below $|B| \lesssim 4$ T suggesting that another carrier response with a much smaller cyclotron mass may be superimposed. The reflection data in Figs. 3(c) and 3(d) also show very different behavior at low fields $|B| \lesssim 4$ T compared to a bulk response. The small humps which appear at fields around $\sim \pm 1$ T in Fig. 3(c) and ~ -1 T in Fig. 3(d) cannot be qualitatively reproduced with any value of bulk carrier concentration, cyclotron mass, or scattering rate.

The addition of a surface state with parameters $\omega_{ps}=41$ cm^{-1}, $\gamma_s=28$ cm^{-1}, and $m_{cs}=0.033m_e$ results in the red solid curves in Figs. 3(a)–3(d) which fit all the data remarkably well. The surface-state cyclotron mass corresponds to a resonance at $B=1.5$ T (for a frequency of 5.24 meV). The scattering rate associated with the surface is substantially larger than that of the bulk, a result which might be expected based on Shubnikov-de Haas measurements on similarly grown samples[15] and linewidths estimated from ARPES data.[11] A conservative lower bound plasma frequency of $\omega_{ps}=20$ cm^{-1} (while concurrently adjusting the surface-state scattering rate to $\gamma_s=16$ cm^{-1}) is estimated where significant deviations well outside the error bars of the data appear, particularly in the real part of the Kerr angle in the vicinity of ± 1 T with deviations of ~ 10 mrad from the data.

From the ARPES measured dispersion of the surface states [see Eq. (A4)],[11] the cyclotron mass given by $\hbar k_f/v_f$ and number density given by $\pi k_f^2/(2\pi)^2$ may be parametrized in terms of the Fermi energy. A mass of $0.033m_e$ corresponds to a Fermi energy of ~ 20 meV above the Dirac point, a number density of 10^{11} cm^{-2}, and corresponding surface plasma frequency of 1.3 cm^{-1}. The bulk plasma fre-

quency corresponds to a Fermi energy of approximately 20 meV above the bulk conduction-band edge which is itself located ~ 200 meV above the Dirac point.

ARPES observations correspond to a large occupation number of the surface states, $n_s \sim 10^{12}$ cm^{-2}.[11] This amount of charge acting on the bulk carriers would deplete the free carriers to a depth $d=n_s/n_b \sim 100$ nm (where n_b is the bulk number density). Since ARPES concurrently observed the bulk bands but the measurement technique is sensitive to depths of only ~ 1 nm, it must be assumed that there is a fixed neutralizing positive surface charge coming from excess Se$^+$ or adsorbed ions, or possibly an intrinsic effect. Therefore, band-bending effects are apparently small in vacuum-cleaved crystals. Samples exposed to ambient conditions show a large n-type doping compared to vacuum-cleaved samples.[20] Since the crystals were grown in a selenium-rich environment, it is possible that the cleaved surfaces contain excess selenium which may also act as capping layers. Such surface chemical doping can move the Dirac point toward the chemical potential and leads to a depletion region in the bulk, presumably with $d < n_s/n_b$. Since the optical penetration depth is much larger than 100 nm at terahertz frequencies,[19] an insulating depletion layer has no significant optical response and the experiment sees the surface carriers only as a modification to the bulk.

More significantly, the surface plasma frequency obtained from the fits to the optical response are about a factor of 15–30 larger than predicted from conventional transport theory based on the ARPES measured surface-state dispersion relation. A possible explanation is that the crystal has multiple surface layers within the optical penetration depth, perhaps separated by interstitial selenium, dividing the crystal into ~ 10 thin flakes which are optically very close but electronically decoupled. The cleave process may favor the region with layers of flakes where these interstitial selenium may be more prevalent offering a weaker link between planes.

Given the unconventional spin-chiral nature of the eigenstates, which imply spin currents perpendicular to the charge currents, an unconventional matrix element for Landau-level transitions may also lead to enhancement of the spectral weight, a possibility that needs further investigation.

As a possible alternative explanation, the structure observed at low field in the optical response of sample 1 may arise from spatial variation in the bulk charge-carrier concentration. Consider the possibility that the optical spot covers a region where two crystallites of different carrier concentrations exist. Modeling this scenario, a simple weighted average of two individual bulk responses without surface states is performed with the following parameters: one bulk response weighted by 0.84 with parameters $\omega_{pb1}=334$ cm^{-1}, $\gamma_{pb1}=6.5$ cm^{-1}, and $m_{cb1}=0.126$ with a second bulk response weighted by (1–0.84) with parameters $\omega_{pb2}=548$ cm^{-1}, $\gamma_{b2}=8.2$ cm^{-1}, and $m_{pb2}=0.148m_e$. The green dashed-dotted curves in Figs. 3(a)–3(d) show all of the salient features of the data which were attributed to the surface states. The difference between the two bulk masses is unexpected for a simple parabolic band near a gapped band edge. The coarse qualitative features of the data may be reproduced by choosing the bulk masses to be the same with the other parameters
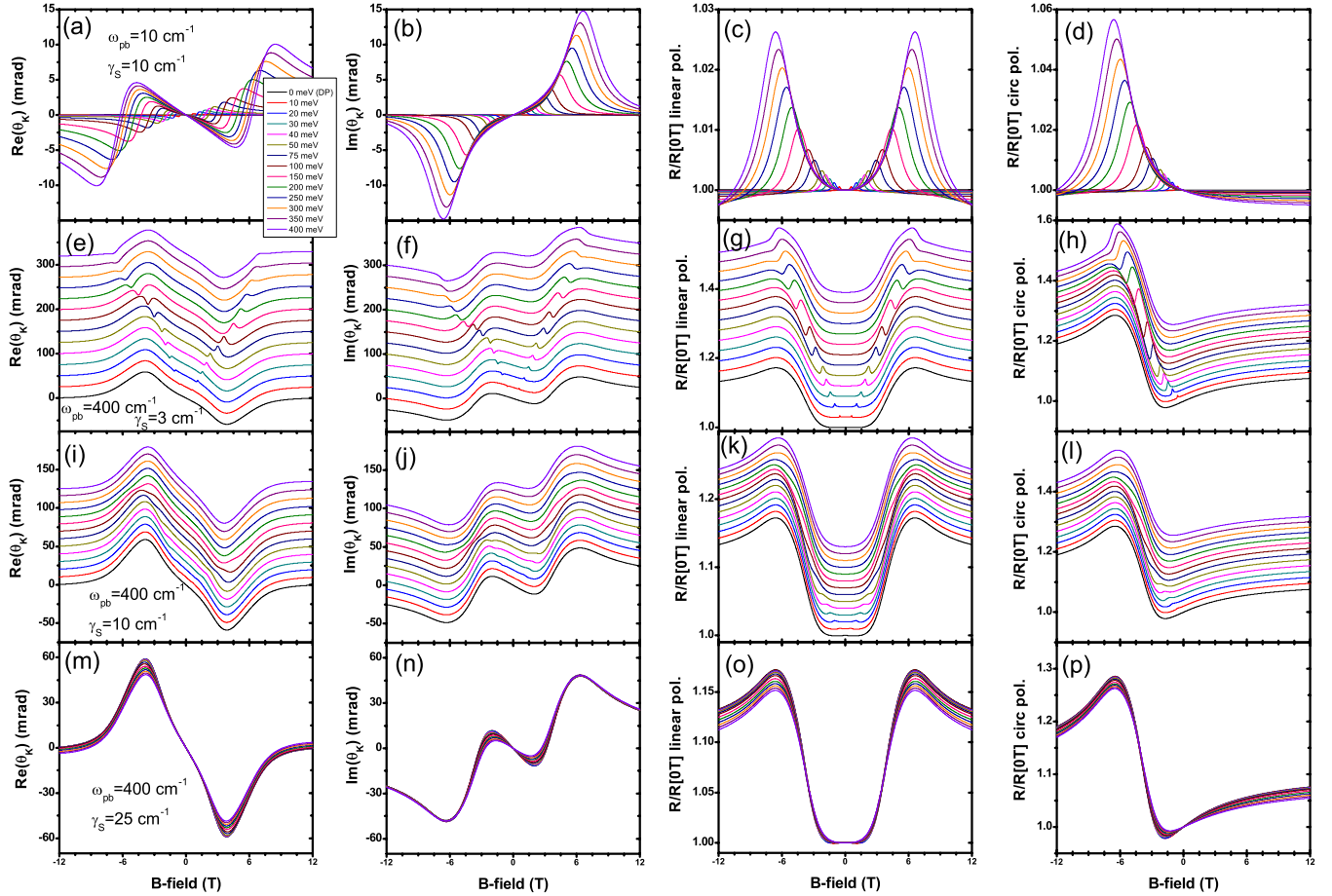
FIG. 4. (Color online) Calculated optical response produced by the bulk properties and the expected surface-state response as measured by ARPES of Bi_2Se_3 as a function of magnetic field for series of surface-state Fermi energies measured above the Dirac point as given in the legend: $E_F = 0$, 10, 20, 30, 40, 50, 75, 100, 150, 200, 250, 300, 350, and 400 meV. The Kerr angle as well as the reflectance (normalized to zero field) in a pure circular or linear state are calculated. Each row of graphs represents a different set of Drude parameters describing the bulk and surface-state response. The second and third row graphs, (e)–(h) and (i)–(l), are offset for clarity such that the Kerr angle is zero and $R/R[0\ T]$ is unity in zero magnetic field. The graphs with the Fermi energy $E_F = 0$ correspond to the Dirac point where there is no contribution from the surface state, only bulk response. All graphs are calculated with a bulk mass $m_{cb} = 0.15 m_e$ and a bulk scattering rate $\gamma_b = 10$ cm^{-1} and using the bulk phonon parameters as measured in Ref. 19. [(a)–(d)] Very low bulk density to demonstrate the response expected from the surface states: $\omega_{pb} = 10$ cm^{-1}, $\gamma_s = 10$ cm^{-1}. (e)–(h) $\omega_{pb} = 400$ cm^{-1}, $\gamma_s = 3$ cm^{-1} (i)–(l) $\omega_{pb} = 400$ cm^{-1}, $\gamma_s = 10$ cm^{-1}. (m)–(p) $\omega_{pb} = 400$ cm^{-1}, $\gamma_s = 25$ cm^{-1}.

chosen similarly although the fits are substantially worse. Therefore, even though the fit is not very good quantitatively, it is possible that a distribution of carrier concentrations may be the culprit giving rise to the observed line shapes.

Perhaps lending more credence to the spatial variation in carrier concentration argument is that a completely different response was measured by a separate sample which was only 2 mm away from sample 1 in the $\sim \varnothing 1.5$ cm as-grown crystal. The measurement results of sample 2 are shown in Figs. 3(e)–3(g). A single bulk response qualitatively describes all the features of the data, as depicted by the blue dashed-dotted curves, whose parameters are $\omega_{pb} = 583$ cm^{-1}, $\gamma_b = 7$ cm^{-1}, and $m_{cb} = 0.145 m_e$. β is assumed zero in calculations in Fig. 3(h). This is a much higher bulk plasma frequency than found for sample 1. Addition of a surface-state response does not improve the fits. However, modeling the bulk carrier concentration variations as was done for sample 1 where one bulk response is weighted by 0.70 with param-

eters $\omega_{pb1} = 583$ cm^{-1}, $\gamma_{b1} = 5.3$ cm^{-1}, and $m_{cb1} = 0.145 m_e$ and a second bulk response weighted by (1–0.70) with parameters $\omega_{pb2} = 250$ cm^{-1}, $\gamma_{b2} = 15$ cm^{-1}, and $m_{cb2} = 0.145 m_e$ yields a good quantitative fit to all three data sets as shown by the green dashed-dotted curves in Figs. 3(e)–3(g). A third sample measured 2 mm away from sample 2 (and 4 mm away from sample 1) yielded the same response as sample 2.

Fourier transform infrared (FTIR) reflectivity measurements in the far-infrared at room temperature on a crystal from the same batch (performed in a similar manner as Ref. 19, Fig. 4) yielded a bulk plasma frequency of 480 cm^{-1} consistent with the Kerr measurements.

Controlling carrier concentrations to well within a factor of ~ 10 over centimeter-sized crystals is very challenging. Using the Kerr and reflectivity measurements, it is not possible to determine whether such a response originates from a distribution of carrier concentration in a single crystallite or
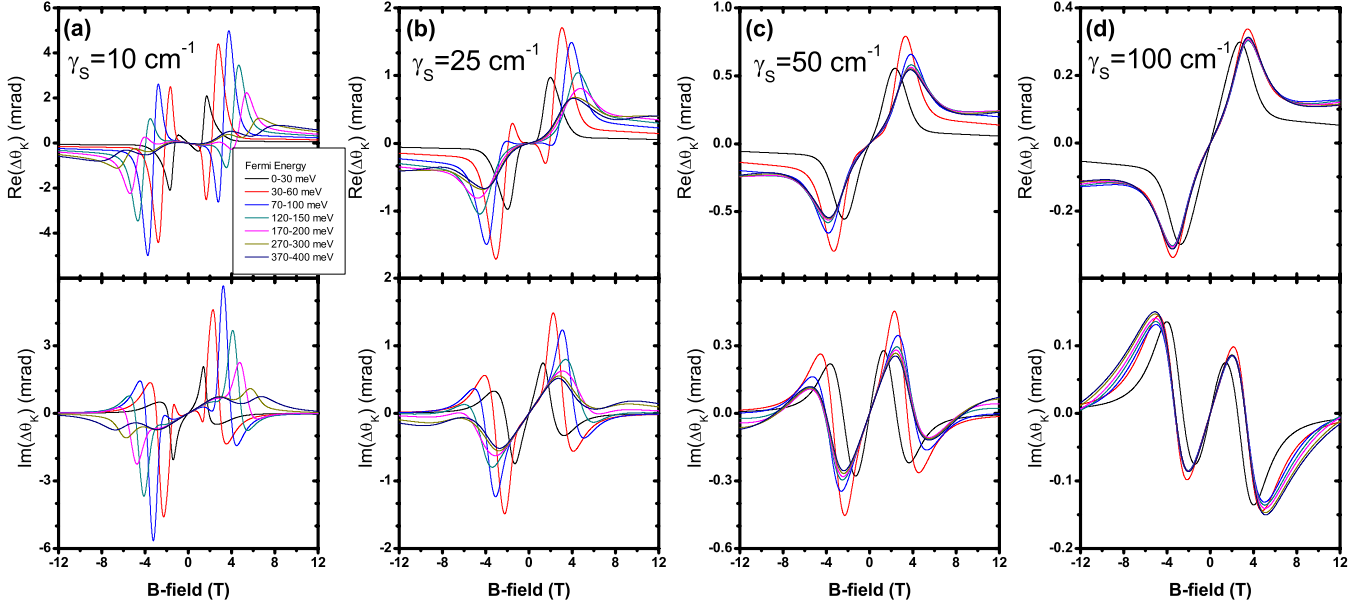
FIG. 5. (Color online) Calculated optical response produced by a hypothetical gate voltage which shifts the Fermi energy of the surface state by 30 meV. The change in Kerr angle produced by this shift at various Fermi energies for a specific surface scattering rate is shown for each column. All graphs are calculated using the bulk phonon parameters measured in Ref. 19 as well as the Drude bulk parameters ω_{pb} =400 cm^{-1}, γ_b=10 cm^{-1}, and m_{cb}=0.15m_e. The surface-state 2D plasma frequency and mass are calculated based on the Fermi level and the measured ARPES dispersion relation (Ref. 11). The surface scattering rates are assumed to be (a) γ_s=10 cm^{-1}, (b) γ_s=25 cm^{-1}, (c) γ_s=50 cm^{-1}, and (d) γ_s=100 cm^{-1}.

the presence of two (or more) crystallites with different concentrations.

B. Other methods to characterize surface states

Using the Kerr measurement technique as a routine diagnostic of sample carrier concentration variation is not feasible since it is resource intensive. Since inhomogeneity is an important general issue, a routine diagnostic tool is required. One method presently being explored utilizes FTIR spectroscopic reflection measurements. As representatively shown in the reflectivity spectral measurements in Fig. 4 of Ref. 19, a large dip occurs at the plasma edge. The frequency location of the dip gives information regarding the carrier concentration. Measurements on different parts of a sample utilizing a small spot size $\sim \varnothing 0.5$ mm in the infrared spectral region is currently being investigated as a diagnostic tool to quantify the degree of carrier-concentration variation.

Another method that may be favorable for observing surface states presently being developed utilizes a gate. If the surface states have a cyclotron mass and optical spectral weight commensurate with the ARPES measured dispersion, the line-fitting procedure as used for the above Kerr and reflection data for discerning the surface state will most likely be extremely difficult with the present signal to noise of the system, even for fairly small surface scattering rates (see Appendix B 1 for details).

By gating, the surface-state optical response can be modulated with negligible effects produced by the bulk. Any modulated signal coming from the bulk would necessarily be due to the screening layer after the depletion layer which is of thickness $\sim 1/k_s$, the Thomas-Fermi screening length. k_s

~ 15 nm at n_b=10^{17} cm^{-3}, a typical carrier concentration. The charge in this layer $n_d \sim n_b/k_s \sim 10^{11}$ cm^{-2} which is much less than the surface-state carrier density. More important, however, is that k_s does not depend on gate voltage and therefore is not modulated. Second, by modulating a gate, signal to noise is expected to increase by over an order of magnitude. Averaging between gate-on and gate-off configurations in fixed field on relatively short-time scales eliminates magnetic field drift issues and minimizes time drift issues. Third, due to this large gain in sensitivity, even very high surface scattering rates should be detectable. Expected signals produced by gating, modeled in Appendix B 2, are expected to be well within experimental capability. Fourthly, the expected Kerr response from the surface states for bulk plasma frequencies ranging from 200 to 600 cm^{-1} have qualitatively the same line shapes. Even with possible carrier inhomogeneities, the detection of surface states is possible by modulating a gate with modest shifts of the surface-state Fermi energy. However, characterization of the surface states will require reasonably homogeneous carrier concentrations. Lastly, developing the technique is a necessary stepping stone for future experiments: measurement of the half-quantized Hall conductivity in topological insulators inside the gap created by a magnetic layer.[7]

V. CONCLUSION

Kerr measurements using heterodyne detection in the terahertz regime are reported. Measurements of a 2DEG GaAs heterostructure prove the system works exceptionally well. Results on Bi$_2$Se$_3$ crystals show that the technique is

sensitive to bulk carrier concentration. For one particular sample, the Kerr and reflectance data are very well described by including surface states. The measured surface spectral weight ω_{ps} (with an associated surface cyclotron mass m_{cs} $=0.033m_e$) is ~20 times larger than expected for a single surface state based on ARPES measurements. Spatial variation in carrier concentration can also qualitatively account for the data. Separation of bulk and surface states may be accomplished in the Kerr geometry with greater sensitivity by incorporating a gate, a proposed next step to clearly separate the bulk and surface-state effects.

APPENDIX A: MULTILAYER RESPONSE ANALYSIS

1. General notation

The formalism for deriving the Fresnel reflection and transmission amplitudes for a system consisting of multiple layers of "dielectric" slabs with thin films at the interfaces are derived for a general number of layers. The model will be applied to two specific cases: a GaAs 2DEG heterostructure with a metallic antireflection coating and a bulk Bi_2Se_3 crystal with a surface state.

Using Maxwell's equations for radiation at normal incidence, boundary conditions on the electric and magnetic field may be applied across any boundary between two dielectric slabs i and $i+1$ of thicknesses db_i and db_{i+1} with bulk complex indices n_i and n_{i+1} and a metallic thin film at the interface with a sheet conductivity of $\sigma_i df_i$, where df_i is the thickness of the film. The vector notation (E^r, E^l) represents right and left traveling waves. The electric field may be expressed in either a linear polarization basis notated as (E_x^r, E_x^l) and (E_y^r, E_y^l) or in a circular polarization basis as (E_+^r, E_+^l) and (E_-^r, E_-^l). To derive the equations generally, we use the notation (E_α^r, E_α^l) to represent one of the polarization basis states y, x, $+$, or $-$.

The matrix $M_{i,\alpha}$ which transfers an arbitrary E-field (E_α^r, E_α^l) across an interface consistent with Maxwell's equations is given by the following:

$$M_{i,\alpha} = \frac{1}{2n_{i+1,\alpha}} \times \begin{pmatrix} n_{i,\alpha} + n_{i+1,\alpha} - y_{i,\alpha} & -n_{i,\alpha} + n_{i+1,\alpha} - y_{i,\alpha} \\ -n_{i,\alpha} + n_{i+1,\alpha} + y_{i,\alpha} & n_{i,\alpha} + n_{i+1,\alpha} + y_{i,\alpha} \end{pmatrix},$$

where the admittance of the thin film is $y_{i,\alpha} = Z_0 \sigma_{i,\alpha} df_i$ and Z_0 is the impedance of free space.

The matrix $K_{i,\alpha}$ transfers an arbitrary oscillating E-field (E_α^r, E_α^l) at frequency ω across a dielectric of thickness db_i and complex index $n_{i,\alpha}$ is given by the following:

$$K_{i,\alpha} = \begin{pmatrix} e^{\imath n_{i,\alpha} db_i \omega/c} & 0 \\ 0 & e^{-\imath n_{i,\alpha} db_i \omega/c} \end{pmatrix}.$$

In general, an incident right traveling wave will be assumed incident on the first interface with a resulting net reflected traveling wave to the left from the first interface and a net right traveling transmitted wave from the last interface. The Fresnel transmission and reflection amplitudes for a stack of dielectrics of m interfaces with thin metallic films are then found by the relation

$$\begin{pmatrix} t_\alpha \\ 0 \end{pmatrix} = M_{m,\alpha} \prod_{i=1}^{m-1} K_{i+1,\alpha} M_{i,\alpha} \begin{pmatrix} 1 \\ r_\alpha \end{pmatrix}.$$

2. GaAs 2DEG

The above formalism can be applied to calculate the Kerr and Faraday angle as well as the reflection and transmission for the calibration sample. A GaAs 2DEG is modeled as a thin metallic sheet whose sheet conductance is described within a simple Drude model located at the interface between vacuum and a GaAs dielectric slab. The backside of the sample consists of an interface between a GaAs dielectric slab and vacuum with an antireflection coating, a thin metallic NiCr film, modeled within a Drude model. The antireflection coating is fully characterized by the dc sheet resistance, $R_\square = 1/(\sigma df)$, since the scattering rate of NiCr is very large compared to the optical frequency. The circular polarization basis is easiest to work with in applied magnetic field.

The parameters are as follows: $n_{1,\pm} = 1$, $n_{2,\pm} = 3.6$, $n_{3,\pm} = 1$, $\omega = 5.24$ meV, $(Z_0 \sigma df)_{1,\pm} = \omega_{ps1}^2/[\gamma_1 - \imath(\omega \pm \omega_{cs1})]$, $db_2 = 0.5$ mm, and $(Z_0 \sigma df)_{2,\pm} = Z_0/R_\square$, where $\omega_{cs1} = eB/(mc)$ is the cyclotron frequency of the 2DEG, $\gamma_1 = e/(m\mu)$ is the scattering rate of the 2DEG, $\omega_{ps1} = 4\pi ne^2/(mc)$ is the plasma frequency of the 2DEG, m is the quasiparticle mass, B is the applied magnetic field, e is the electronic charge, c is the speed of light, μ is the mobility, and n is the 2D number density.

The Fresnel amplitudes $r_\pm$ and $t_\pm$ as a function of n, μ, $R_\square$, m, and B are then found by substituting the above parameters into the following equations:

$$\begin{pmatrix} t_+ \\ 0 \end{pmatrix} = M_{2,+} K_{2,+} M_{1,+} \begin{pmatrix} 1 \\ r_+ \end{pmatrix},$$

$$\begin{pmatrix} t_- \\ 0 \end{pmatrix} = M_{2,-} K_{2,-} M_{1,-} \begin{pmatrix} 1 \\ r_- \end{pmatrix}. \quad \text{(A1)}$$

The reflection R and transmission T for unpolarized light, reflection $R_\pm$ and transmission $T_\pm$ for circularly polarized light, and the Faraday θ_F and Kerr θ_K angles are calculated from the Fresnel amplitudes as follows:

$$R_\pm = r_\pm r_\pm^*,$$

$$T_\pm = t_\pm t_\pm^*,$$

$$R = (1/2)(R_+ + R_-),$$

$$T = (1/2)(T_+ + T_-),$$

$$\tan(\theta_F) = \iota(t_+ - t_-)/(t_+ + t_-),$$

$$\tan(\theta_K) = \iota(r_+ - r_-)/(r_+ + r_-), \tag{A2}$$

where " $*$ " notates the complex conjugate.

3. Bi$_2$Se$_3$

Bi$_2$Se$_3$ is modeled as a surface-state Drude response on top of a very thick bulk slab whose response consists of a free-carrier Drude term with two phonon resonances. The bulk phonon parameters as well as the approximate cyclotron mass and scattering rate have previously been measured.[19]

The bulk dielectric function is given by the following:

$$\epsilon^{\pm} = -\frac{\omega_{pb}^2}{\omega(\omega \pm \omega_{cb} - \iota\gamma_b)} + \sum_{j=1}^{2} \frac{S_j}{\omega_j^2 - \omega(\omega - \iota\gamma_j)} + \epsilon_\infty, \tag{A3}$$

where j enumerates the phonon oscillators, ω_j is the TO phonon frequency, S_j is the phonon spectral weight, a subscript b refers to bulk electrons, ϵ_∞ is the dielectric constant at higher infrared frequencies, ω_{pb} is the unscreened plasma frequency for free electrons: $\omega_{pb}^2 = 4\pi N_b e^2/m_b^*$, where N_b, e, and m_b^* are concentration, charge, and an effective mass of electrons; γ_b and γ_j are the damping rates; $\omega_{cb} = eB/(m_{cb}c)$ is the bulk cyclotron frequency, where B is magnetic field, m_{cb} is bulk cyclotron mass, and c is the speed of light.

The reported phonon parameters are $\omega_1 = 67$ cm^{-1}, $S_1 = 3.94 \times 10^5$ cm^{-2}, $\gamma_1 = 5$ cm^{-1}, $\omega_2 = 134$ cm^{-1}, $S_2 = 7056$ cm^{-2}, $\gamma_2 = 2$ cm^{-1}, and $\epsilon_\infty = 25.6$.[19] The reported bulk cyclotron mass is approximately $m_{cb} \approx 0.16m_e$, where m_e is the bare electron mass and the approximate bulk scattering rate $\gamma_b \approx 8$ cm^{-1}, although both are left as parameters in the model. The relation $m_b^* = m_{cb}$ is assumed true so that N_b (or equivalently the plasma frequency, ω_{pb}) is the third adjustable parameter associated with the bulk response. With these values, $\epsilon_\pm$ is a function of radiation frequency ω and applied magnetic field B, and the bulk plasma frequency ω_{pb}, mass m_{cb}, and scattering rate γ_b.

Since the surface-state penetration depth is $\sim$nm which is much less than the optical wavelength for terahertz radiation, the surface state may be modeled as a two-dimensional sheet of charge. The model of a 1-cm-thick Bi$_2$Se$_3$ slab in vacuum with a Drude surface-state response at the first interface are as follows: $n_{1,\pm} = 1$, $n_{2,\pm} = \sqrt{\epsilon_\pm}$, $n_{3,\pm} = 1$, $(Z_0\sigma df)_{1,\pm} = \omega_{ps}^2/[\gamma_s - \iota(\omega \pm \omega_{cs})]$, $db_2 = 1$ cm, $(Z_0\sigma df)_{2,\pm} = 0$, where $\omega_{cs} = eB/(m_s c)$ and $\omega_{ps} = (4\pi/c)n_s e^2/m_s$. Even for very low densities of bulk carriers, the properties of the last interface do not affect the reflected optical response due to the large attenuation within the thick bulk crystal.

Inserting the above values into Eqs. (A1) give the reflection and transmission Fresnel amplitudes as a function of ω, B, ω_{pb}, γ_b, m_{cb}, ω_{ps}, γ_s, and m_{cs}. The Fresnel amplitudes are also given in Ref. 19, Eqs. 4–6.

Digitizing and fitting the reported ARPES measured dispersion relation for the surface state from Ref. 11 gives the following functional form:

$$E_F = 2.02k_f + 10.44k_f^2, \tag{A4}$$

where the Fermi energy E_F is measured in electron volt above the Dirac point and k_f is measured in per angstrom. n_s (or ω_{ps}), m_{cs}, v_f, and k_f are fully determined by the dispersion relation for any given Fermi energy.

Using the dispersion relation, R, T, $R_\pm$, $T_\pm$, θ_F, and θ_K are calculated from Eq. (A2) as a function of ω, B, ω_{pb}, γ_b, m_{cb}, E_F, and γ_s.

APPENDIX B: EXPECTED OPTICAL SIGNATURES OF SURFACE STATES BASED ON ARPES MEASUREMENTS

1. Expected Kerr and reflectance signals

Figure 4 shows calculated results for the expected Kerr and reflection signals, both from linearly and circularly polarized light, as a function of magnetic field for various Fermi energies ranging from 0 to 400 meV above the Dirac point. All graphs in Fig. 4 are calculated assuming a bulk cyclotron mass value of $m_{cb} = 0.15m_e$ and bulk scattering rate $\gamma_b = 10$ cm^{-1}. The surface-state plasma frequency ω_{ps} and cyclotron mass m_{cs} are determined by the ARPES measured dispersion [Eq. (A4)] for a specific surface Fermi energy. Each row of graphs are calculated with a different bulk plasma frequency ω_{pb} and surface scattering rate γ_s.

The optical response for a pure surface state with $\gamma_s = 10$ cm^{-1} is shown in Figs. 4(a)–4(d) (the response of the bulk is negligible for $\omega_{pb} = 10$ cm^{-1}). All signals are well within the capability of the Kerr measurements. Note that Re(θ_K) and Im(θ_K) show antiresonantlike and resonantlike behavior. The cyclotron mass and strength of the response increase with Fermi energy. The reflection in purely circularly polarized light depicted in Fig. 4(d) exhibits a hump in the cyclotron resonant active mode. The reflection in linear polarization depicted in Fig. 4(c) (composed of equal amounts of left and right circularly polarized light) shows two humps since there is an active cyclotron mode in positive and negative fields. The qualitative structure of the Kerr and reflection signals is instructive since they appear superimposed on larger bulk responses at larger values of ω_{pb}.

Row 2 of figures, namely, Figs. 4(e)–4(h), show the optical response expected with a bulk plasma frequency of $\omega_{pb} = 400$ cm^{-1} and surface scattering rate $\gamma_s = 3$ cm^{-1}. The bulk is depicted by the black curves since no carriers are in the surface state at the Dirac point, $E_F = 0$. The curves are offset for clarity: in zero magnetic field, the Kerr angle is always zero and the normalized reflection is always equal to unity. With such a low surface scattering rate, the sharpness of the surface-state response is seen clearly superimposed upon the bulk response.

The next row of figures, Figs. 4(i)–4(l), shows the effect of increasing the surface scattering rate to $\gamma_s = 10$ cm^{-1}. Again, the curves are offset for clarity. Although the effect of surface states is discernible in many of the curves, fitting the line shapes with the current signal to noise of the measurement system becomes problematic.

The last row of figures, Figs. 4(m)–4(p), shows the effect of increasing γ_s to 25 cm^{-1}. Fitting line shapes on this level to discern the effects produced by surface states is not conducive to the current measurement scheme.

2. Expected Kerr signals with application of a gate

A gate which concurrently allows ample throughput optical power while inducing negligible Kerr or Faraday rotation has been accomplished. High resistivity silicon substrates with a 300 nm film of SiO$_2$ were ion implanted with peak concentrations $>10^{19}$/cm^3 resulting in a density profile thickness of ~ 0.3 μm. Characterization of these devices show very small Faraday rotation up to 8 T, excellent optical throughput power, no carrier freeze out, and large break down voltages. The devices are currently being used to gate large chemical-vapor deposition grown graphene in similar magneto-optical experiments.

Estimates of the shift in Fermi energy of the surface state associated with the application of electric fields commensurate with the typical breakdown voltages of SiO$_2$ depends on the Fermi energy. For currently available samples the surface-state charge density is sufficiently large that it dominates the charge transfer to the sample due to the gate. As a result the band offset is reasonably given by the change in the Fermi energy due to the charge transfer to the surface states. The depletion depth in the bulk is then given to a good approximation by $d^2 = 2U_0 \epsilon_0 / e^2 n_b$ (where U_0 is the energy above the Dirac point and ϵ_0 is the bulk static dielectric constant). Therefore, the net charge which one can add or subtract from the surface state without breakdown of the insulator is very nearly equal to the maximum allowable charge transfer with the application of a gate. Using a maximum applicable electric field value of 3.3×10^8 V/m for SiO$_2$ is equivalent to a net change in surface-charge density of 7×10^{12} cm^{-2}. Based on the ARPES measured dispersion, this gives a shift of Fermi energy $\Delta E_F \approx 90$ meV at $E_F = 0$, $\Delta E_F \approx 30$ meV at $E_F = 200$ meV, and $\Delta E_F \approx 15$ meV at $E_F = 350$ meV. Since the gate voltage can be reverse biased as well, roughly twice these changes can be realized. The resulting depletion depth decouples the surface states, but is small enough that the insulating depletion layer is optically invisible at terahertz frequencies.

Based on these estimates, the application of a gate is chosen to produce a change in Fermi energy of $\Delta E_F = 30$ meV. Figure 5 shows the expected Kerr signals predicted by the ARPES measured surface-state properties with bulk parameters of $\omega_{pb} = 400$ cm^{-1}, $\gamma_b = 10$ cm^{-1}, and $m_{cb} = 0.15 m_e$. Each graph shows Fermi-level shifts of 0–30 meV, 30–60 meV, 70–100 meV, 120–150 meV, 170–200 meV, 270–300 meV, and 370–400 meV. Graphs (a)–(d) show the effects of increasing the surface scattering rate from 10 to 100 cm^{-1}. Reflectance measurements are not very sensitive, showing that $R/R[0 \text{ T}] \lesssim 0.5\%$ for $\gamma_s = 25$ cm^{-1} and $\lesssim 0.1\%$ for $\gamma_s = 50$ cm^{-1}.

Changes in Kerr angle at the level of 0.1 mrad is very reasonably obtainable in this configuration. It should be noted that the signals are maintained at these general levels even for higher bulk plasma frequencies up to 600 cm^{-1}.

[1] L. Fu, C. L. Kane, and E. J. Mele, Phys. Rev. Lett. **98**, 106803 (2007).

[2] J. E. Moore and L. Balents, Phys. Rev. B **75**, 121306 (2007).

[3] R. Roy, Phys. Rev. B **79**, 195322 (2009).

[4] L. Fu and C. L. Kane, Phys. Rev. B **76**, 045302 (2007).

[5] B. A. Bernevig, T. L. Hughes, and S. Zhang, Science **314**, 1757 (2006).

[6] B. A. Bernevig and S.-C. Zhang, Phys. Rev. Lett. **96**, 106802 (2006).

[7] X.-L. Qi, T. L. Hughes, and S.-C. Zhang, Phys. Rev. B **78**, 195424 (2008).

[8] H. Zhang, C. Liu, X. Qi, X. Dai, Z. Fang, and S. Zhang, Nat. Phys. **5**, 438 (2009).

[9] D. Hsieh, D. Qian, L. Wray, Y. Xia, Y. S. Hor, R. J. Cava, and M. Z. Hasan, Nature (London) **452**, 970 (2008).

[10] D. Hsieh et al., Science **323**, 919 (2009).

[11] Y. Xia et al., Nat. Phys. **5**, 398 (2009).

[12] D. Hsieh et al., Phys. Rev. Lett. **103**, 146401 (2009).

[13] P. Roushan, J. Seo, C. V. Parker, Y. S. Hor, D. Hsieh, D. Qian, A. Richardella, M. Z. Hasan, R. J. Cava, and A. Yazdani, Nature (London) **460**, 1106 (2009).

[14] Y. S. Hor, J. G. Checkelsky, D. Qu, N. P. Ong, and R. J. Cava, arXiv:1006.0317 (unpublished).

[15] N. P. Butch, K. Kirshenbaum, P. Syers, A. B. Sushkov, G. S. Jenkins, H. D. Drew, and J. Paglione, Phys. Rev. B **81**, 241301 (2010).

[16] J. G. Checkelsky, Y. S. Hor, R. J. Cava, and N. P. Ong, arXiv:1003.3883 (unpublished).

[17] G. S. Jenkins, D. C. Schmadel, and H. D. Drew, Rev. Sci. Instrum. **81**, 083903 (2010).

[18] A. Raymond, J. L. Robert, and C. Bernard, J. Phys. C **12**, 2289 (1979).

[19] A. B. Sushkov, G. S. Jenkins, D. C. Schmadel, N. P. Butch, J. Paglione, and H. D. Drew, arXiv:1006.1008 (unpublished).

[20] J. G. Analytis, J.-H. Chu, Y. Chen, F. Corredor, R. D. McDonald, Z. X. Shen, and I. R. Fisher, Phys. Rev. B **81**, 205407 (2010).